High-Resolution Solid-State NMR Relaxometry as a Kinetic Tool for the Study of Ultrafast Proton Transfers in Crystalline Powders. Dimethyldibenzotetraaza[14]annulene

Christof-G. Hoelger, Bernd Wehrle,[1] Hans Benedict, and Hans-Heinrich Limbach*

Institut für Organische Chemie, Freie Universität Berlin, Takustrasse 3, 14195 Berlin, F.R.G.

Received: August 4, 1993®

NMR relaxometry combined with high-resolution solid-state NMR techniques has been explored as a kinetic tool for the study of ultrafast proton transfers in solids. Rate constants of proton transfer are obtained in the milli- to nanosecond time scale by analysis of the longitudinal spin–lattice relaxation times T_1 of heteronuclei located in such a way that their dipolar interaction to the mobile protons is modulated by the transfer process. The T_1 measurements are facilitated by proton cross-polarization (CP), magic angle spinning (MAS), and proton decoupling during the detection period. In contrast to the study of static powders, the CPMAS method also provides the equilibrium constants of proton transfer necessary to obtain the rate constants from the T_1 values. Heteronuclear longitudinal relaxation in the presence of proton transfer is described in the theoretical section for the cases of (i) static powders, (ii) powders rotating at the magic angle, and (iii) powders where longitudinal relaxation is isotropically averaged by magnetization transfer. In case i relaxation is multiexponential and difficult to evaluate. In case iii relaxation is truly exponential and characterized by a single longitudinal relaxation time T_1, related in a straightforward way to the dipolar interaction and the equilibrium and rate constants of proton transfer. This case is, however, difficult to realize experimentally, by contrast to the MAS case ii. As shown theoretically, in this casee relaxation is quasi-monoexponential and governed in very good approximation by the same T_1 values as in case iii. Therefore, rate constants of ultrafast proton transfers can be obtained from CPMAS T_1 measurements as long as other relaxation mechanisms are not operative. As an example, a dynamic ^{15}N CPMAS NMR study of polycrystalline dimethyldibenzotetraaza[14]annulene (DTAA: 1,8-dihydro-6,13-dimethyldibenzo[*b,i*]-$^{15}N_4$-(1,4,8,11)-tetraazacyclotetra-deca-4,6,11,13-tetraene) is presented. As shown previously, DTAA is subject to an intramolecular double proton transfer between two tautomers which are degenerate in the gas phase but inequivalent in the crystalline solid. Longitudinal ^{15}N relaxation of DTAA under MAS conditions has been monitored at 2.1 and 7 T in a large temperature range and was found to be monoexponential. Deuteration in the mobile proton sites drastically reduced the relaxation rates, proving that the ^{15}N T_1 values of DTAA are dominated by proton-transfer-induced dipolar relaxation. A T_1 minimum of protonated DTAA was observed around 350 K. Using the theory of case iii, this observation allowed us to convert the T_1 values measured into rate constants of proton transfer in the milli- to nanosecond time scale and to determine the ^1H–^{15}N distances. The validity of this approach was verified by additional experiments performed on static powders and complete data analyses in terms of cases i and ii. At 7 T a small contribution to T_1 arising from a proton-transfer-induced modulation of the chemical shift anisotropy (CSA) had to be taken into account. In the milli- to microsecond time scale the rate constants obtained by ^{15}N T_1 analysis agree very well with those obtained by ^{15}N CPMAS line shape analysis. The resulting Arrhenius curve shows a small deviation from linearity. In conclusion, relaxometry of powdered crystalline or of disordered solids under MAS conditions constitutes a reliable technique for obtaining rate constants of ultrafast proton transfers in organic solids.

Introduction

For a long time, dynamic liquid-state NMR spectroscopy[2-4] has been a powerful tool for studying the dynamics and the thermodynamics of proton-transfer reactions including their kinetic hydrogen/deuterium isotope effects.[5-7] The oncome of high-resolution solid-state NMR methods of spin $^1/_2$ nuclei under the conditions of cross-polarization (CP), magic angle spinning (MAS), proton decoupling, and variable temperature[8-11] made it possible to extend such studies to the solid state. A variety of different proton-transfer reactions in organic solids have been detected in recent years employing ^{15}N CPMAS NMR[12-20] as well as ^{13}C CPMAS NMR spectroscopy.[21-25] When the proton-transfer barriers are large enough, characteristic line shape changes occur at low temperatures in the CPMAS NMR spectra. In this case, rate constants of proton transfer can be obtained in the millisecond range by NMR line shape analysis[12,15-19] and in the second time scale by polarization-transfer experiments.[20,21] When the proton transfer is very fast with respect to the NMR time scale, rate constants can unfortunately no longer be obtained by line shape analysis although the observation of temperature-dependent equilibria still gives evidence of a double-minimum potential of the proton motion.[12,14,15]

The dynamic range problem of solid-state NMR for the study of ultrafast proton and deuteron transfers can be solved when these processes modulate homonuclear dipolar interactions in the case of ^1H and the quadrupole interaction in the case of ^2H, which leads to characteristic values of the longitudinal relaxation times.[3] Thus, several authors have studied proton and deuteron dynamics in single crystals via the measurement of ^1H and/or ^2H T_1 relaxation times of the mobile protons or deuterons.[26-31] Recently, a ^1H T_1 relaxation study of a static powdered solid was reported where the longitudinal ^1H relaxation is governed by the heteronuclear dipolar ^1H–^{14}N interaction.[32] However, only energies of activation of proton transfer but no rate constants could be derived because the T_1 values can be converted into rate constants only if the equilibrium constants are also known. In the case of single crystals the latter can be obtained from line

* To whom correspondence should be addressed.

® Abstract published in *Advance ACS Abstracts,* January 1, 1994.

0022-3654/94/2098-0843$04.50/0 © 1994 American Chemical Society

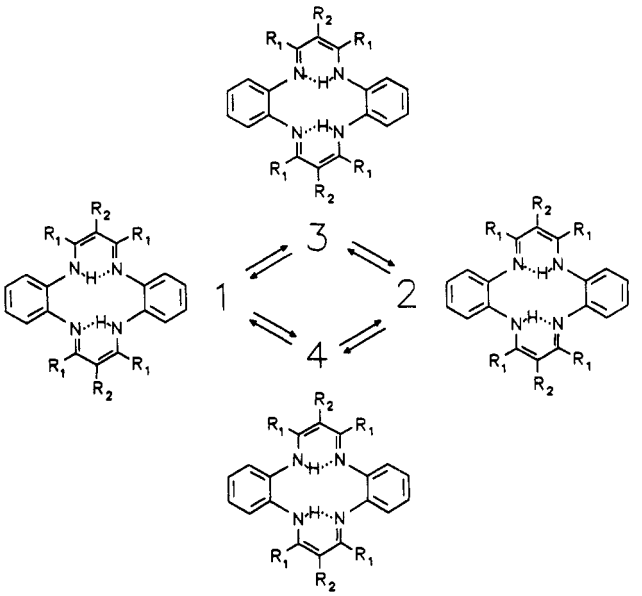

Figure 1. Tautomerism of dibenzotetraaza[14]annulenes. DTAA: R_1 = H and R_2 = CH_3. TTAA: R_1 = CH_3 and R_2 = H.

positions, but in the case of crystalline powders sophisticated two-dimensional experiments are required.[33] A disadvantage of ^1H relaxometry is also the case that longitudinal relaxation of mobile and immobile protons is averaged by spin diffusion, which sometimes makes it difficult to separate proton-transfer-induced relaxation from other mechanisms.

Since selective T_1 data as well as accurate equilibrium constants can be obtained by CPMAS experiments of heteronuclei dipolar coupled to the jumping protons or deuterons, it is surprising that this method has not yet been exploited. The scope of this paper is, therefore, to explore the possibility of obtaining rate constants of solid-state proton transfers from such measurements. We show that this goal can be achieved, for example, in the case of ^{15}N CPMAS NMR of $^{15}NH\cdots X$ proton-transfer systems which substantially widens the possibilities of dynamic high-resolution NMR in the solid state.

As an example, we present a study of the solid-state tautomerism of dimethyldibenzotetraaza[14]annulene (DTAA: 1,8-dihydro-6,13-dimethyldibenzo(*b,i*)-$^{15}N_4$-(1,4,8,11)-tetraazacyclotetra-deca-4,6,11,13-tetraene, Figure 1), which was discovered several years ago.[15] This compound contains two intramolecular hydrogen bonds embedded in six-membered H-chelate units of the malonaldehyde type. In the case of DTAA, the two tautomers to which the trans structures **1** and **2** of Figure 1 have been assigned[15] are not degenerate because of solid-state perturbations. The tautomers **3** and **4** in Figure 1 are not directly observable but are possible intermediates of the exchange processes between tautomers **1** and **2**. It must be noted that for the related TTAA evidence for the formation of all four tautomers has been obtained.[14] Preliminary rate constants of the process **1** to **2** in DTAA were obtained by ^{15}N CPMAS line shape simulations at 1.5 T in a relatively small temperature range.[15] Here, this range is extended by line shape analysis at higher field strengths and ^{15}N T_1 experiments.

In the following theoretical section, we adapt the existing theory of homonuclear dipole–dipole relaxation in the presence of solid-state proton transfers[27-29] for the heteronuclear case. Both static powders and powders rotating at the magic angle are considered. After the experimental section, the results of all dynamic ^{15}N CPMAS NMR experiments are described, analyzed, and discussed. Assumptions made in order to simplify the longitudinal relaxation analysis under MAS conditions are corroborated by analysis of the frequency-dependent longitudinal relaxation in the case of the static powders. It is shown that the kinetic results

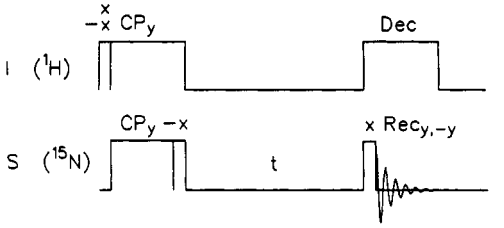

Figure 2. Pulse sequence for CPMAS NMR T_1 measurements proposed by Torchia.[36] The equilibrium magnetization is zero because of phase cycling of the first proton 90° pulse and of the receiver phase.

are consistent, which establishes ^{15}N CPMAS relaxometry as a tool for the study of millisecond to nanosecond proton transfers to and from nitrogen.

Experimental Part

^{15}N-enriched DTAA was prepared from *o*-phenylenediamine according to the procedure of Lorch et al.[34] modified for small-scale synthesis with isotopes; $^{15}N_2$-*o*-phenylenediamine was prepared as described previously.[15]

The ^{15}N CPMAS NMR measurements were performed at 9.12 MHz (2.1-T cryomagnet) and 30.41 MHz (7-T cryomagnet) using NMR spectrometers Bruker CXP 100 and MSL 300. For the 30.41-MHz measurements a 5-mm DOTY high-speed CPMAS probe head was used, and for the 9.12-MHz measurements a standard 7-mm Doty CPMAS probe was used. The rotors were loaded with 10–15 mg of DTAA. During the high-speed measurements at 30.41 MHz, separate rotor bearing and driving gas supplies were employed where only the bearing gas was thermostated using a homemade heat exchanger.[35] For our probe, this procedure leads only to small temperature gradients.[14c] The sample temperatures were monitored by adding into the rotor a capsule containing a small amount (0.8–1.5 mg) of ^{15}N-enriched TTAA (tetramethyldibenzotetraaza[14]annulene-$^{15}N_4$, Figure 1). TTAA contributes four sharp lines to the ^{15}N CPMAS spectra whose position is highly sensitive to temperature.[14b,c] All spectra were referenced to external solid $^{15}NH_4Cl$ (95%).

The ^{15}N T_1 relaxation times were measured between 225 and 437 K using the usual pulse sequence described by Torchia where no proton decoupling is applied during the equilibration period t (Figure 2).[36] Because of the phase cycling scheme illustrated in Figure 1, the longitudinal relaxation can be described by[36]

$$M = M_0 \exp(t/T_1) \qquad (1)$$

The spectra were taken using 90° pulse widths of 3.6 μs at 2.1 T and 5 μs at 7 T. Spinning frequencies of 6.6–8 kHz at 7 T and of 2 kHz at 2.1 T allowed to obtain rotational sideband-free spectra. Each T_1 data point was calculated from a set of 6–10 spectra with different delays between 1 ms and a time close to T_1. Between 500 and 1000 scans were accumulated for each spectrum.

Line shape measurements at 9.12 MHz were performed as described previously.[15] The 30.41-MHz spectra were taken with rotor frequencies of 8.8 kHz in order to avoid complications from spinning sidebands. Spectral artifacts were minimized using a T_1 pulse sequence with 5 ms as waiting time.[37]

Theoretical Section

In this section we describe how information concerning the thermodynamics and the kinetics of proton transfer of the type

$$\mathbf{1} \equiv AH\cdots X \rightleftarrows \mathbf{2} \equiv A\cdots HX \qquad (2)$$

can be obtained by high-resolution CPMAS NMR spectroscopy and relaxometry of the heteronuclei S = A, X embedded in powdered solids. The equilibrium constant characterizing eq 2

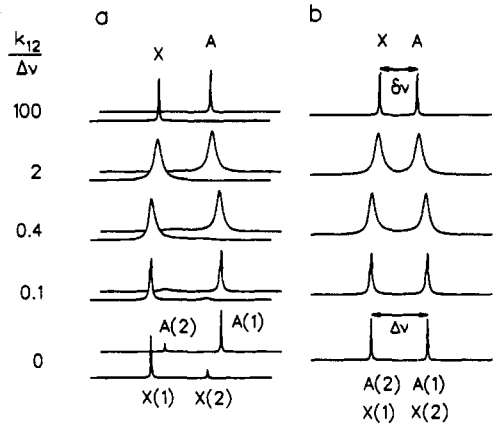

Figure 3. Calculated spectra for two single spins A and X located in an asymmetric molecule subject to exchange between two isomers. The equilibrium constant $K_{12} = k_{12}/k_{21}$ of the isomerism was set to a value of 0.2 in all spectra. The values of k_{12} increase from the bottom to the top. For further explanation see text. (a) Spectra calculated for the case that the chemical shifts of all nuclei are different. (b) Spectra calculated for the case where A and X are in similar chemical environments, i.e., for the case of the validity of eqs 6 and 7.

is defined by

$$K_{12} = x(2)/x(1) = k_{12}/k_{21} \tag{3}$$

k_{ij} is the rate constant of the reaction from state i to j and $x(i)$ the mole fraction of state i. As a convention, we assign in this paper the index 1 to the dominantly populated state. It is convenient to define a correlation time τ_c of the proton motion as follows

$$\tau_c^{-1} = k_{12} + k_{21} = \{(1 + K_{12})/K_{12}\}k_{12} \tag{4}$$

Generally, it is assumed that the dependence of k_{12} on temperature T is given by an Arrhenius law

$$k_{12} = A_{12} \exp(E_{a_{12}}/RT) \tag{5}$$

where $E_{a_{12}}$ is the energy of activation and A_{12} the frequency factor of the forward reaction (eq 2).

The proton transfer of eq 2 leads to a modulation of the chemical shifts of A and X as well as to a modulation of the dipolar AH and XH interaction. The expected line shape changes arising from the modulation of the isotropic chemical shifts have been calculated previously[18,19] and are shown in Figure 3. Figure 3a depicts the case where all isotropic chemical shifts are different. In the slow-exchange region four lines are observed at $\nu_A(1)$, $\nu_A(2)$, $\nu_X(1)$, and $\nu_X(2)$. The intensity ratio of lines A(2) to A(1) and of lines X(2) to X(1) corresponds to K_{12}. The intensity ratio of lines A(i) to X(i), $i = 1, 2$, should be one. Note, however, that in a CPMAS NMR experiment deviations from unity can be observed arising from differing cross-polarization dynamics of A and X. When the rate constants increase, the lines broaden and coalesce. In the fast-exchange region, the line positions are given by

$$\nu_A = x(1)\,\nu_A(1) + (1 - x(1))\nu_A(2) \tag{6}$$

$$\nu_X = x(1)\,\nu_A(1) + (1 - x(1))\nu_X(2) \tag{7}$$

The special case where

$$\nu_A(1) \approx \nu_X(2) \quad \text{and} \quad \nu_A(2) \approx \nu_X(1) \tag{8}$$

i.e.

$$\nu_A(1) - \nu_A(2) = \nu_X(2) - \nu_X(1) = \Delta\nu \tag{9}$$

is shown in Figure 3b. Only two lines are observed in the slow-exchange range at a distance $\Delta\nu$. As the rate constants are increased, the two lines broaden, shift toward each other, and sharpen again. The equilibrium constant K_{12} can be obtained from the splitting $\delta\nu$ at high temperatures using the equation[14]

$$K_{12} = \frac{\Delta\nu - \delta\nu}{\Delta\nu + \delta\nu} \tag{10}$$

which can easily be derived from eqs 2, 3, and 6–9. As shown in the results section, the ^{15}N CPMAS NMR spectra of DTAA can be explained in terms of Figure 3.

Let us now analyze the longitudinal relaxation times T_1 of the spins S = A, X determined by the experiment of Figure 2. As shown below, relaxation may depend on whether MAS is applied during the whole experiment or not. Let S = A, X be dipolar coupled to the mobile proton designed in the usual way as spin I. In the equilibration period the modulation of the dipolar coupling by the proton transfer according to eq 1 provides a source of longitudinal relaxation of the S spins according to Figure 4a because of the geometrical change of the proton I. $\gamma_S(i)$ denotes the bond angle AIX in state i, $\alpha_S = \gamma_S(1) - \gamma_S(2)$ the jump angle of the SI vector, and $r_{SI}(i)$ the distance between S and I in state i.

The T_1 value of a spin S in a pair of two dipolar coupled spins IS in a single crystal is given in SI units by[3]

$$\frac{1}{T_{1S}} = \gamma_I^2\gamma_S^2\hbar^2(\mu_0/4\pi)^2(I(I+1))\left[\frac{1}{12}J_0(\omega_I - \omega_S) + \frac{3}{2}J_1(\omega_S) + \frac{3}{4}J_2(\omega_I + \omega_S)\right] \tag{11}$$

where γ_i, $\hbar$, and μ_0 have the usual meanings and ω_i is the Larmor frequency of spin i. The spectral density $J_m(\omega)$ is the Fourier transform of the correlation function $F^m(t)$.[26] In principle, the $J_m(\omega)$ depends on the angle $\theta_{SI}(i)$ between the internuclear distance vector $r_{SI}(i)$ in the tautomeric form i and the applied magnetic field B_0, as shown in Figure 4b. For a single orientation, Andrew and Lantanowitz derived expressions for $J_m(\omega)$ for the homonuclear case where I and S are protons.[27] In a straightforward way we obtain for the heteronuclear case where spins S = A, X are relaxed by I for a single orientation:

$$J_0 = 2R_0\frac{K_{12}}{(1 + K_{12})^2}\frac{\tau_c}{1 + (\omega_I - \omega_S)^2\tau_c^2} \tag{12}$$

$$R_0 = (\xi^0_{SI}(1) - \xi^0_{SI}(2))^2, \quad \xi^0_{SI}(i) = \frac{1 - 3\cos^2\theta_{SI}(i)}{r^3_{SI}(i)} \tag{13}$$

$$J_1 = 2R_1\frac{K_{12}}{(1 + K_{12})^2}\frac{\tau_c}{1 + \omega_S\tau_c^2} \tag{14}$$

$$R_1 = (\xi^1_{SI}(1) - \xi^1_{SI}(2))^2; \quad \xi^1_{SI}(i) = \frac{\sin\theta_{SI}(i)\cos\theta_{SI}(i)}{r^3_{SI}(i)} \tag{15}$$

$$J_2 = 2R_2\frac{K_{12}}{(1 + K_{12})^2}\frac{\tau_c}{1 + (\omega_I + \omega_S)^2\tau_c^2} \tag{16}$$

$$R_2 = (\xi^2_{SI}(1) - \xi^2_{SI}(2))^2, \quad \xi^2_{SI}(i) = \frac{\sin^2\theta_{SI}(i)}{r^3_{SI}(i)} \tag{17}$$

In order to describe relaxation of a powdered static solid and a solid rotating with the frequency Ω_r at the magic angle $\mu = 54.7°$ between B_0 and Ω_r, it is useful to relate the angles $\theta_{SI}(1)$ and $\theta_{SI}(2)$ to the angles θ, ϕ, and ψ defined in Figure 4b. θ characterizes the angle between the vector $r_{SI}(1)$ and the rotation axis Ω_r. ψ is the phase of the rotation. $\psi = 0$ when $r_{SI}(1)$ is located in the plane of the vectors B_0 and Ω_r. Crystallites characterized by the same vector $r_{SI}(1)$ may differ with respect to the orientation of the vector $r_{SI}(2)$. $r_{SI}(2)$ forms a cone around $r_{SI}(1)$ with a cone angle α_S and the phase ϕ. $\phi = 0$ when $r_{SI}(2)$ lies in the plane

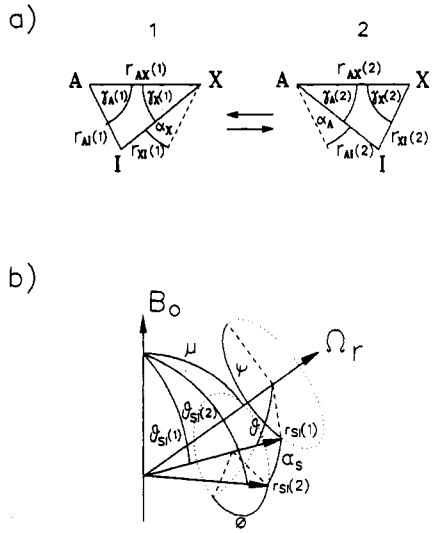

Figure 4. (a) Nuclear arrangement of spin I jumping between two spins S = A, X. (b) Explanation of angles used in eqs 12–19.

defined by the vectors Ω_r and $r_{SI}(1)$. Using simple geometric relations, we obtain

$$\theta_{SI}(1) = \arccos(\cos\theta\cos\mu - \sin\theta\sin\psi\sin\mu) \quad (18)$$

$$\theta_{SI}(2) = \arccos\{\cos\alpha_S\cos\theta_{SI}(1) + \sin\alpha_S(\cos\phi\cos\theta\cos\psi\sin\mu - \cos\phi\sin\theta\cos\mu + \sin\phi\sin\psi\sin\mu)\} \quad (19)$$

In the absence of molecular motions and spin diffusion between different crystallites, the decay of the longitudinal magnetization $M(t)$ of a static powder is then given by a sum of single-exponential decays of the individual molecular orientations characterized by the angles θ, ϕ, ψ:

$$M_S(t) = N\int_0^{\pi}\int_0^{2\pi} M(t=0,\theta,\phi,\psi=0) \exp\left(-\frac{t}{T_{1S}(\theta,\phi,\psi=0)}\right)\sin\theta\,d\theta\,d\phi \quad (20)$$

N is a normalization factor. It is not possible to derive simple analytical expressions for the multiexponential function $M_S(t)$ by combining eqs 11–20. Equation 20 can, however, easily be calculated numerically.

In the case of magic angle spinning the situation is simplified. As long as the nuclear motions are fast as compared to the coherent magic angle spinning process—which is generally the case—we do not expect an interference between the two processes. Then, all spin packets characterized by the same values of θ and ϕ and differing only in the phase ψ will experience an averaged common value $T_1(\theta,\phi)$ which can be calculated according to

$$\frac{1}{T_{1S}(\theta,\phi)} = \frac{1}{2\pi}\int_0^{2\pi}\frac{1}{T_{1S}(\theta,\phi,\psi)}\,d\psi \quad (21)$$

The resulting decay of the longitudinal magnetization under MAS conditions is then given by

$$M_S(t) = N\int_0^{\pi}\int_0^{2\pi} M_S(t=0,\theta,\phi)\exp\left(-\frac{t}{T_{1S}(\theta,\phi)}\right)\sin\theta\,d\theta\,d\phi \approx M_S(t=0)\exp\left(-\frac{t}{T_{1S}^{mas}}\right) \quad (22)$$

Equation 22 assumes that in contrast to the case of the static powder relaxation under MAS conditions is monoexponential in practice and characterized by an effective longitudinal relaxation time T_1^{mas}. This assumption will be corroborated below theoretically and experimentally.

Finally, if one assumes spin diffusion between different crystallites or an isotropic molecular motion faster than longitudinal relaxation but much slower than the proton transfer, the decay of the longitudinal magnetization becomes truly monoexponential, characterized by the "isotropic" relaxation time

$$\frac{1}{T_{1S}^{iso}} = \frac{1}{2\pi}\int_0^{\pi}\int_0^{2\pi}\int_0^{2\pi}\frac{1}{T_{1S}(\theta,\phi,\psi=0)}\sin\theta\,d\theta\,d\phi$$

$$= \frac{1}{30}\gamma_I^2\gamma_S^2\hbar^2(\mu_0/4\pi)^2(I(I+1))R_{SI}\frac{4K_{12}}{(1+K_{12})^2}\times \left[\frac{\tau_c}{1+(\omega_I-\omega_S)^2\tau_c^2}+\frac{3\tau_c}{1+\omega_S^2\tau_c^2}+\frac{6\tau_c}{1+(\omega_I+\omega_S)^2\tau_c^2}\right] \quad (23)$$

For the case of the homonuclear relaxation among mobile protons a similar equation was derived previously.[27] The geometrical factor R_{SI} in eq 23 is related to the parameters defined in Figure 4a by

$$R_{SI} = \sum_I r_{SI}^{-6}(1) + r_{SI}^{-6}(2) + r_{SI}^{-3}(1)\,r_{SI}^{-3}(2)(1-3\cos^2\alpha_S),\quad S = A, X \quad (24)$$

The sum is taken over all neighboring spins I, which contribute to T_{1S}.

It is interesting to note that eq 23 is independent of whether K_{12} or its inverse $\bar{K}_{12} = K_{21} = 1/K_{12}$ is introduced since τ_c is invariant to this change and since

$$K_{12}/(1+K_{12})^2 = \bar{K}_{12}/(1+\bar{K}_{12})^2 \quad (25)$$

Therefore, neglecting possible small differences between the quantities R_{AI} and R_{XI} the two lines in Figure 3b will be characterized by the same T_1 value.

Experimentally, the values T_1^{mas} are measured. The data analysis of T_1^{iso} is, however, much easier. Therefore, we set in approximation

$$T_{1S}^{mas} = f(k_{12},K_{12},r_{SI}(1),r_{SI}(2),\alpha_S) \approx T_{1S}^{iso} = f(k_{12},K_{12},R_{SI}) \approx T_1 \quad (26)$$

As discussed above, it is possible to obtain the value of K_{12} directly from the CPMAS NMR spectra using eq 10 which leaves only k_{12} and R_{SI} as unknowns. In a narrow temperature region where k_{12} can be described by an Arrhenius law, the activation energy $E_{a_{12}}$ can be calculated from the slope of the curve ln T_1 vs $1/T$. Equation 23 predicts that T_{1S} passes through a minimum at a given value of the correlation time τ_c which is determined by the Larmor frequencies ω_S and ω_I. From the known value of $T_{1S,min}$ the unknown factor R_{SI} can be obtained. Once the minimum is known, the frequency factor A_{12} can be obtained or each T_{1S} value can be converted into a value of k_{12} without the need of eq 5. Since k_{12} is also the parameter extracted from the low-temperature line shape analysis, both methods can then be directly compared.

In order to estimate the systematic error made introduced by the assumption of eq 26, we calculated the magnetization decay curves of a powder rotating at the magic angle using eqs 12–21 for various parameter sets. The resulting multiexponential decays were found to be monoexponential as assumed by eq 22, and T_1^{mas} was obtained by nonlinear least-squares fitting. At the same time the values of T_1^{iso} were calculated using eq 23. The ratios T_1^{mas}/T_1^{iso} obtained are plotted in Figure 5a as a function of the hydrogen bond angle $\gamma = \gamma_A(1) = \gamma_X(2)$ defined in Figure 4. In Figure 5b, the same ratio is plotted as a function of τ_c for different values of γ. In the dynamic range covered T_1^{mas} is always only a few percent larger than T_1^{iso}, and the ratio T_1^{mas}/T_1^{iso} remains fairly constant besides a small reduction when

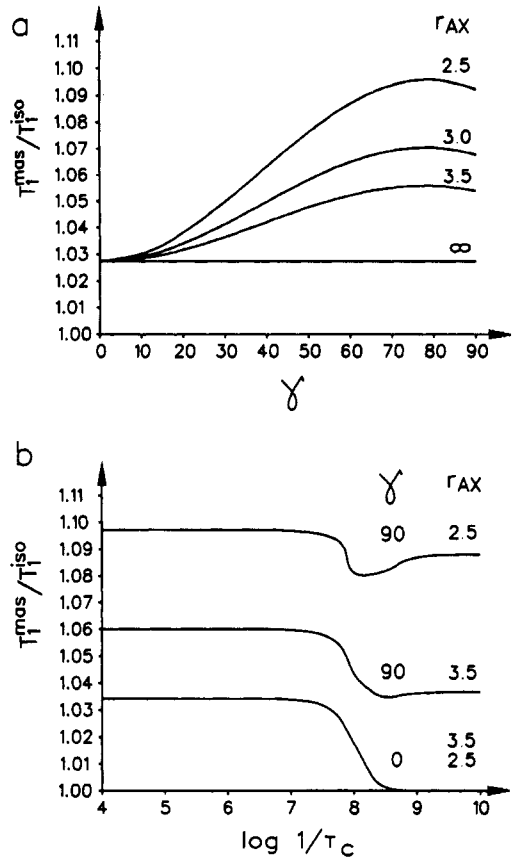

Figure 5. (a) Ratio T_1^{mas}/T_1^{iso} vs the angle $\gamma = \gamma_A(1) = \gamma_X(2)$ defined in Figure 4 for different ratios of $r_{AX}/r_{AI}(1)$, log $1/\tau_c = 7.8$. (b) Ratio T_1^{mas}/T_1^{iso} vs τ_c for different geometries according to Figure 4. $K_{12} = 1$, $\omega_S = 9.12$ MHz, $\omega_I = 90.02$ MHz, $r_{AI}(1) = 1$ Å, values r_{AX} in Å. The calculations were performed assuming the validity of eqs 30 and 31.

the ^{15}N Larmor frequency is of the order of $1/\tau_c$. The small systematic difference is negligible in view of the 100-fold change of the absolute T_1 values in the range covered. In the experimental case of DTAA presented below, we estimate the systematic error introduced by eq 26 to about 0.1 kJ mol^{-1} for the energy of activation $E_{a_{12}}$ and 0.02 for the frequency factor log A_{12}. The systematic error of the geometrical factor R is also smaller than the experimental error. Note, however, that a rigorous simultaneous fit of all magnetization decay curves measured in the whole range of temperatures in terms of eq 22 is tedious but possible.

At high magnetic fields the ^{15}N relaxation times may also be influenced by a proton-transfer-induced modulation of the chemical shift anisotropy (CSA). In principle, CSA and dipolar relaxation interfere with each other. However, in the first approximation, we assume that both contributions are additive

$$1/T_1 \approx 1/T_1^{d} + 1/T_1^{csa} \tag{27}$$

This approximation will hold especially if the CSA term is small. It can be written in the form

$$\frac{1}{T_{1S}^{csa}} = (C\omega_s)^2 \frac{4K_{12}}{(1+K_{12})^2}\left[\frac{\tau_c}{1+\omega_S^2\tau_c^2}\right] \tag{28}$$

where C is a constant depending on the CSA and proportional to the square of the magnetic field B_0.[3]

Results and Discussion

Kinetics and Thermodynamics of the DTAA Tautomerism Studied by Total ^{15}N CPMAS NMR Line Shape Analysis. Since the rate constants of the tautomerism of DTAA obtained previously by ^{15}N CPMAS line shape analysis of 6.082-MHz

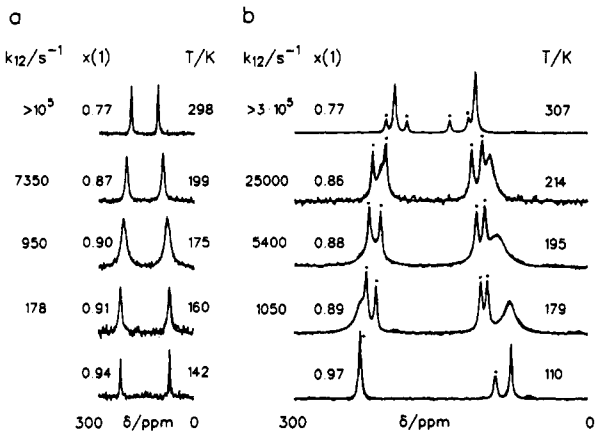

Figure 6. Superposed experimental and calculated ^{15}N CPMAS NMR spectra of 95% ^{15}N-enriched DTAA at 9.12 MHz/2.1 T (a) and 30.41 MHz/7 T (b) as a function of temperature. Reference: external $^{15}N_4Cl$. x_1 is the probability of the dominant tautomer and k_{12} the forward rate constant. The spectra are scaled in frequency units to show the influence of the different field strength. (a) 6–14-ms cross-polarization times, 7-kHz sweep width, 2.7-s repetition time, spinning speeds 2 kHz. Number of scans 3000 on average. The line width in the absence of exchange was taken from the spectra at 142 K. (b) Sharp peaks marked with an asterisk arise from the presence of the chemical shift thermometer TTAA (Figure 1).[14] 2–6-ms cross-polarization time, 7-kHz sweep width, 3.3-s repetition time, spinning speeds 8.8 kHz. Number of scans 1000 on average.

spectra were preliminary, we measured additional data by repeating experiments at 9.12 and 30.41 MHz where the dynamic range of the method is larger. These experiments were also done in order to reach the milli- to microsecond time scale where line shape analysis and relaxometry can be directly compared. Some typical spectra are shown in Figure 6a,b. As described in the experimental section, a small amount of TTAA (see Figure 1) was added as a chemical shift thermometer to the sample measured at 30.41 MHz, leading to the four sharp temperature-dependent lines in Figure 6b marked by asterisks. By simulation of these lines both the sample temperatures and the line widths in the absence of exchange were determined. At low temperatures DTAA contributes two sharp lines to the spectra with the separation $\Delta\nu$. The high field line arises from the protonated nitrogen atoms and the low field line from the nonprotonated atoms. The lines broaden with increasing temperature, move inward, and sharpen again. As the temperature is further increased, the reduced line separation $\delta\nu$ decreases further. These line shape changes follow those of Figure 3, i.e., are typical for the presence of two unequally populated interconverting tautomeric states $\mathbf{1} \equiv N_AH\cdots N_X \rightleftharpoons \mathbf{2} \equiv N_A\cdots HN_X$.

Using eq 10, the equilibrium constants K_{12} of the tautomerism were calculated from the line separations in the temperature range between 225 and 436 K. They are assembled in Table 1. The low-temperature value $\Delta\nu = 154.7$ ppm was taken from the 110 K spectrum. A linear dependence of ln K_{12} vs $1/T$ was observed (Figure 7) described by

$$K_{12} = 1.16 \exp(-412.5/T) \tag{29}$$

from which a reaction enthalpy of $\Delta H_{12} = 3.4 \pm 0.08$ kJ mol^{-1} and a reaction entropy of $\Delta S_{12} = 1.24 \pm 0.1$ J K^{-1} mol^{-1} are calculated. These values agree very well with the values of of $\Delta H_{12} = 3.8$ kJ mol^{-1} and $\Delta S_{12} = 2$ J K^{-1} mol^{-1}, which were reported previously.[15] The reaction entropy is minimal as expected for a reaction where only two protons are transferred. The observation of a smooth van't Hoff curve in Figure 7 indicates the absence of a phase transition in the temperature range covered. Therefore, an order/disorder transition expected in the case of a dependence of the K_{12} values of a particular molecule on the tautomeric states of neighboring molecules is absent. The potential curves of the proton motion of the individual molecules

TABLE 1: Equilibrium Constants of the DTAA Tautomerism in the Solid State

T (K)	δν (ppm)	K_{12}	T (K)	δν (ppm)	K_{12}	T (K)	δν (ppm)	K_{12}
220	107.2	0.182[a]	269	91.1	0.258[b]	348	73.4	0.356[a]
225	106.3	0.185[b]	272	90.5	0.262[a]	349	73.5	0.356[a]
228	104.7	0.192[b]	278	90.8	0.260[a]	351	73.1	0.358[a]
230	105.0	0.191[b]	278	90.3	0.263[b]	356	71.8	0.366[a]
235	103.1	0.200[b]	285	87.6	0.277[a]	361	70.8	0.372[a]
239	99.9	0.215[a]	288	87.9	0.275[b]	364	70.2	0.376[a]
241	100.9	0.210[b]	292	86.0	0.285[a]	366	70.0	0.377[a]
242	100.6	0.212[b]	300	84.5	0.294[b]	373	68.6	0.385[a]
249	99.1	0.219[b]	306	82.5	0.304[b]	377	67.8	0.390[a]
251	98.3	0.223[b]	316	80.7	0.314[a]	385	66.3	0.400[a]
256	96.7	0.231[b]	318	80.2	0.317[a]	391	65.6	0.404[a]
256	95.9	0.235[a]	326	78.5	0.327[a]	404	62.7	0.423[a]
259	96.2	0.233[b]	333	77.6	0.332[a]	419	60.1	0.440[a]
260	95.1	0.238[b]	337	76.0	0.341[a]	429	58.3	0.452[a]
263	93.5	0.246[b]	344	74.9	0.348[a]	436	57.0	0.462[a]

[a] 30.41-MHz data. [b] 9.12-MHz data.

TABLE 2: Rate Constants of DTAA Tautomerism in the Solid State

T (K)	k_{12} (s^{-1})	T (K)	k_{12} (s^{-1})	T (K)	k_{12} (s^{-1})
160	178[b]	179	1050[c]	193	4970[c]
162	125[a]	180	1570[c]	195	5400[c]
163	250[b]	185	2100[c]	199	7350[b]
171	638[b]	187	2480[c]	199	5850[c]
173	377[a]	189	1650[a]	205	12000[c]
175	638[b]	189	3200[c]	214	~25000[c]

[a] ^{15}N CPMAS NMR line shape analysis at 6.082 MHz according to ref 15. [b] ^{15}N CPMAS NMR line shape analysis at 9.12 MHz. [c] ^{15}N CPMAS NMR line shape analysis at 30.41 MHz.

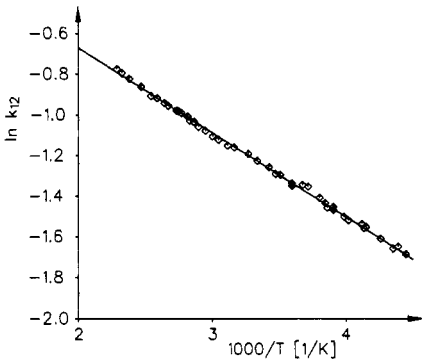

Figure 7. van't Hoff diagram of the tautomerism of solid DTAA.

are, therefore, decoupled in good approximation and are independent of temperature.

The fact that in the fast-exchange regime only two lines are observed in the ^{15}N CPMAS NMR spectra of solid DTAA indicates that the two NH···N proton-transfer units of DTAA are characterized by the same equilibrium constant. This means that only two tautomeric states are observed for DTAA, to which the structures **1** and **2** shown in Figure 1 are assigned. In these states, the van der Waals interactions between the labile protons are minimized. In the gas-phase states **1** and **2** are degenerate; in the solid state, the degeneracy is lifted by solid-state interactions. The protons jump stepwise between states **1** and **2** involving states **3** and **4** as intermediates; this follows by analogy to TTAA where the latter are directly observed.[14]

The rate constants obtained by line shape analysis are listed in Table 2. Assuming an Arrhenius law, we obtain the frequency factors and activation energies listed in Table 3. These data are discussed later in more detail.

Relaxation Time Measurements. The ^{15}N T_1 relaxation times of DTAA were measured at 9.12 and 30.41 MHz under MAS conditions in a wide temperature range; in addition, some measurements were performed at 30.41 MHz for DTAA partially

TABLE 3: T_1 Relaxation Times and Rate Constants of the DTAA Tautomerism in the Solid State

T (K)	T_1 (s)	k_{12} (10^6 s^{-1})	T (K)	T_1 (s)	k_{12} (10^6 s^{-1})
		30.41 MHz			
277	~50	0.61	356	2.18	16.7
285	19.5	1.58	361	1.84	20.9
292	17.1	1.82	364	2.27	16.0
316	7.2	4.1	366	1.97	19.1
318	6.4	5.0	373	1.35	36.0
326	4.9	6.4	377	1.37	34.7
333	3.7	9.0	385	1.17	*a*
337	3.0	11.4	391	1.14	*a*
344	2.02	18.3	404	1.18	*a*
348	2.40	14.8	419	1.46	126
349	2.36	17.5	429	1.04	*a*
351	2.57	13.8	436	1.47	131
		9.12 MHz			
225	68	0.051	306	1.32	3.05
228	59	0.059	316	0.85	5.20
235	41	0.086	324	0.79	5.75
241	33	0.108	333	0.63	8.23
242	28	0.127	336	0.60	9.06
249	12.9	0.279	346	0.44	*a*
251	13.4	0.270	355	0.46	*a*
256	12.4	0.291	358	0.54	22.7
259	8.1	0.449	370	0.56	27.3
260	9.1	0.400	373	0.56	27.3
263	7.3	0.501	379	0.65	38.9
269	5.9	0.625	392	0.79	59.8
278	4.0	0.935	403	0.87	75.8
288	2.3	1.65	413	0.84	72.9
299	1.6	2.46	425	0.92	94.0
300	1.7	2.31			

[a] Since $T_1 < T_{1,min}$ no rate constant can be calculated.

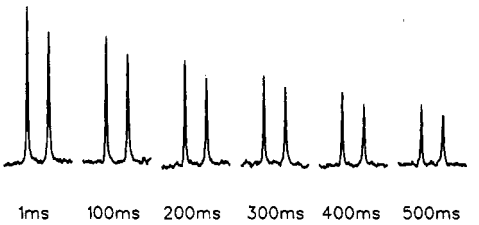

Figure 8. ^{15}N CPMAS T_1 experiment performed on solid DTAA at 9.12 MHz at 353 K under MAS conditions. Spectra between 275 and 50 ppm, reference external $^{15}NH_4Cl$.

deuterated (deuterium fraction $D \approx 0.8$) in the mobile proton sites. A typical 9.12-MHz experiment performed at $D = 0$ and 353 K is shown in Figure 8. As predicted by eq 23, we obtain the same values for both lines. Note that common T_1 values could also result from a moderately fast spin diffusion between ^{15}N atoms, in view of the 95% enrichment with this isotope.[20,21] The T_1 values measured at $D = 0$ are assembled in Table 3 and are plotted in Figure 9 in a logarithmic scale as a function of $1/T$. As can be inferred from Figure 9, deuteration in the mobile proton sites drastically increases the relaxation times which proves that the ^{15}N T_1 values of DTAA are dominated by proton-transfer-induced dipolar relaxation. At 9.12 MHz and $D = 0$ this relaxation mechanism is even the only one as shown in the following. The appearance of a T_1 minimum at about 350 K allowed us to obtain the activation energy $E_{a_{12}}$ of proton transfer, the frequency factor A_{12}, and the geometric factor R_{SI} by nonlinear least-squares fitting of the data to eq 23 (Figure 9a). Next, we tried to fit the T_1 values at 30.41 MHz with the same parameter set. This led to a small systematic disagreement between the experimental data (Figure 9b) and the calculated curve of Figure 9c. Fitting the 30.41-MHz data directly to eq 23 leads to the same activation parameters but to a slightly larger geometric factor R_{SI}, which was unsatisfactory. The disagreement could be overcome by including a term arising from proton-induced CSA relaxation according to eqs 27 and 28 where only the constant C was adapted.

TABLE 4: Arrhenius Parameters of the Tautomerism of DTAA in the Solid State

temp range (K)	E_a (kJ/mol)	$\log(A_{12}/s^{-1})$	method[e]
$179 \le T \le 214$	27.0 ± 1.2	10.9 ± 0.3	TLA (30.41 MHz)[a]
$160 \le T \le 199$	25.3 ± 0.3	10.5 ± 0.1	TLA (9.12 MHz)[a]
$162 \le T \le 189$	23.9 ± 3.8	9.9 ± 1.3	TLA (6.08 MHz)[a,b]
$225 \le T \le 425$	30.2 ± 0.4	11.7 ± 0.1	T_1(9.12 MHz), C_{csa} = 0,[c] R_{NH} = 0.605 ± 0.017[d]
$277 \le T \le 425$	32.0 ± 0.4	11.98 ± 0.14	T_1(9.12 MHJz), C_{csa} = 0,[c] R_{NH} = 0.628 ± 0.018[d]
$277 \le T \le 436$	32.4 ± 1.2	12.0 ± 0.14	T_1(30.41 MHz), C_{csa} = 0,[c] R_{NH} = 0.868 ± 0.047[d]
$225 \le T \le 436$	30.5 ± 0.5	11.7 ± 0.1	T_1(9.12 MHz/30.41 MHz), C_{csa} = 54 ± 4,[c] R_{NH} = 0.601 ± 0.023[d]
$277 \le T \le 436$	32.0 ± 0.8	11.9 ± 0.1	T_1(9.12 MHz/30.41 MHz), C_{csa} = 56 ± 4,[c] R_{NH} = 0.610 ± 0.025[d]

[a] These values differ slightly from the preliminary values reported previously:[15] $k_{12} \approx 10^7 \exp(-14.7 \text{ kJ mol}^{-1}/RT)\ s^{-1}$). [b] Values obtained by the data set reported in ref 15 by neglecting the uncertain low-temperature value. [c] Value of C/ppm in eq 16 arisingh from longitudinal relaxation via the chemical shift anisotropy at 7 T. [d] Unit is Å^{-6}. [e] TLA = total line shape analysis.

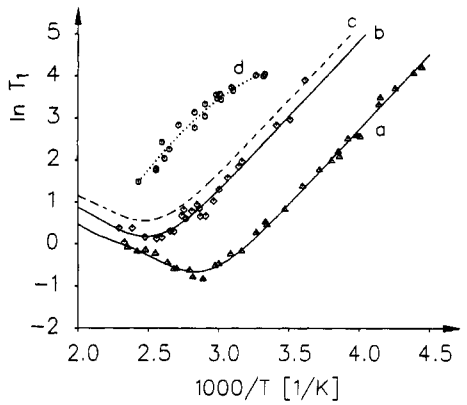

Figure 9. Dependence of the ^{15}N longitudinal relaxation times T_1 of polycrystalline DTAA powders rotating at the magic angle as a function of the inverse temperature and at two deuterium fractions D in the mobile proton sites. (a) 9.12 MHz, D = 0; (b) 30.41 MHz, D = 0; solid lines calculated according to eqs 23, 27, and 28 using the parameters $E_{a_{12}}$ = 30.2 kJ mol^{-1}, $\log A_{12} = 11.7$, $R = 0.605 \times 10^{-60}$ m^{-6}, C = 0 at 9.12 MHz, and C = 56 ppm at 30.41 MHz; (c) Calculated with the same parameters exc ept that C = 0 ppm at 30.41 MHz. (d) $D \approx 0.8$, 30.41 MHz; the dotted line is only a guide for the eye.

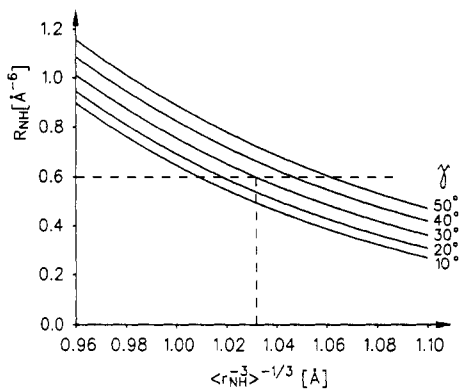

Figure 10. Evaluation of the NH distance from the geometrical factor R_{SI} for DTAA.

Finally, the 9.12- and 30.41-MHz data were fitted simultaneously to eqs 23, 27, and 28 by adapting $E_{a_{12}}$, A_{12}, R_{SI}, and C leading to the solid lines in Figure 9a,b.

All fit parameters are assembled in Table 4. In the last stage of the data analysis we used the best values of R_{SI} = 0.61 Å^{-6} and C = 56 ppm to interconvert the experimental T_1 values into k_{12} values for better comparison with the data obtained by total line shape analysis. These constants are also listed in Table 3. The data obtained at $D \approx 0.8$ were not analyzed because of the low deuterium content and difficulties with dedeuteration during the experiments. We estimate that the ^{15}N T_1 values are still dominated by the transfer of the hydrogen isotopes and not by other motions; however, it is not easy to separate the CSA contribution from relaxation induced by mobile dueterons and mobile residual protons. Furthermore, at very long T_1 values, intermolecular spin diffusion with protonated DTAA molecules play a role leading to the observed change of the slope of log $T_1(D \approx 0.8)$ vs $1/T$.

Geometrical Information from the CPMAS ^{15}N T_1 Measurements Performed on DTAA. In this section we show that the geometrical factor R_{SI} obtained experimentally is in good agreement with the molecular structure of DTAA which further corroborates the above data analysis. For this purpose we set in the geometric model of Figure 4a $\gamma_A(1) = \gamma_X(2) = \gamma$, $\gamma_A(2) = \gamma_X(1) = \gamma'$, $r_{AX}(1) = r_{AX}(2) = r_{NN}$, $r_{AI}(1) = r_{XI}(2) = r_{NH}$ and $r_{AI}(2) = r_{XI}(1) = r'_{NH}$. Then, the jump angle defined in Figure 4 can be expressed as

$$\alpha_N = \gamma - \gamma' = \gamma - \arccos(r_{NN} - r_{NH} \cos \gamma)/r'_{NH} \quad (30)$$

r_{NN} is the distance of the two ^{15}N atoms in the NH···N hydrogen bond, r_{NH} the short ^1H–^{15}N distance, and r'_{NH} the long H···N bond. The latter can be expressed by

$$r'_{NH} = (r_{NN}^2 - 2r_{NN}r_{NH} \cos \gamma - r_{NH}^2)^{0.5} \quad (31)$$

Unfortunately, a crystallographic analysis of DTAA is not available. However, in good approximation, we can use the data obtained by Goedken et al.[38] for TTAA which indicate that $r_{NN} \approx 2.69$ Å and $\gamma \approx 30°$. The latter value is only approximate because of the difficulties in localizing the mobile hydrogen atoms by X-ray crystallographic analysis. By combining eqs 30 and 31 with eq 24, it is possible to calculate the approximation N–H distance of the mobile protons as a function of γ. The result is shown in Figure 10. As usual, distances obtained from dipolar couplings are average cubic values, i.e., $\bar{r}_{NH} = \langle \overline{r_{NH}^{-3}} \rangle^{-1/3}$ which do not necessarily coincide exactly with those obtained by other methods. The deviations are such that distances are obtained which are smaller than expected for the equilibrium position in the case where the potential function is harmonic. Larger values may be obtained in the presence of residual motional averaging processes or of a strongly anharmonic potential at high degrees of excitation. For R_{SI} = 0.61 Å^{-6} and γ = 30° we obtain r_{NH} = 1.03 ± 0.01 Å from the 9.12-MHz data set, which is a very reasonable result. Changing the value of γ did not significantly change the value of r_{NH} as illustrated in Figure 10. On the other hand, if we apply the value of R = 0.868 Å^{-6} (Table 4) calculated from the 30.41-MHz data without taking into account the CSA correction, we obtain r_{NH} = 0.98 ± 0.01 Å, which is still of the correct order but seems to be too small for moderately strong intramolecular NH···N hydrogen bonds. Thus, the resulting NH distance is about 1.03 Å, demonstrating that dipole–dipole relaxation between the ^{15}N nucleus and the moving proton is the exclusive relaxation mechanism at 9.12 MHz and the dominant mechanism at 30.41 MHz where CSA relaxation makes a small contribution. If experiments were performed only at high magnetic fields, a minor systematic error would arise in the determination of the rate constants as the data would not permit separation of the CSA contribution. Thus, it is evident that ^{15}N T_1 measurements should be made at lower rather than at higher field strengths.

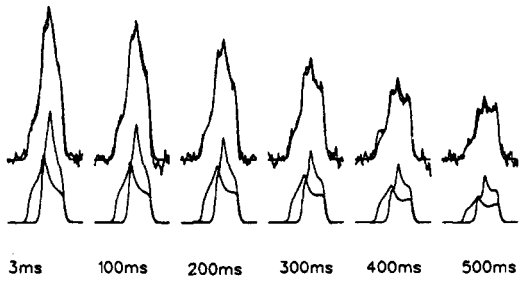

Figure 11. ^{15}N CP T_1 experiment performed on the static powder of DTAA at 9.12 MHz and 353 K. The spectra are shown between 650 and −250 ppm. The letters A and X refer to the notation in Figures 3, 4, and 6. The calculated spectra were obtained with the following parameters whose derivation is described elsewhere.[39] Chemical shift values of nonprotonated nitrogen atoms in the slow-exchanger regime: σ_{11} = 487 ppm, σ_{22} = 256 ppm, σ_{33} = −47 ppm. Chemical shift values of protonated nitrogen atoms in the slow-exchange regime: σ_{11} = 169 ppm, σ_{22} = 80 ppm, σ_{33} = −11 ppm. Short and long nitrogen–hydrogen distances: r_{NH} = 1.04 Å and r'_{NH} = 1.92 Å. Euler angles relating the NH vectors to the corresponding chemical shift tensors: α_D = 28°, β_D = 90° for r_{NH} and α_D = 57°, β_D = 90° for r'_{NH}. Euler angles relating the two CSA tensors: α_{csa} = 39°, β_{csa} = 0°, γ_{csa} = 0°. Dynamic parameters as described in the text.

Effects of the Orientation Dependence of the Longitudinal Relaxation. In order to estimate the error made by analyzing the longitudinal ^{15}N relaxation of static or rotating DTAA powders in terms of eq 23 which is strictly valid only for the isotropic average, we proceeded as follows. In Figure 11 the results of a longitudinal ^{15}N CP T_1 experiment performed on the static DTAA powder at 353 K, D = 0 and 9.12 MHz are shown. These results can be directly compared with those of Figure 8 where all conditions were the same except that MAS was employed. The spectra of Figure 11 consist of two subspectra for the two chemically inequivalent ^{15}N atoms exhibiting features typical for nonaxial CSA tensors. Such experiments are very tedious because of the broadness of the lines and the associated low signal-to-noise ratio. The line shapes change slightly with the delay time. In particular, as can be inferred from Figure 11, the low field and center parts of both subspectra decay faster than the high field parts. These changes can be explained in terms of a dependence of the longitudinal relaxation on the orientation of the various crystallites with respect to the magnetic field B_0. As shown in Figure 11, the spectra could be simulated taking into account eqs 6–19 and the additional parameters given in the legend of Figure 11. The latter were derived by line shape analysis of DTAA powders protonated and deuterated in the mobile proton sites. These experiments will be described elsewhere.[39]

The resulting integral magnetizations for both the MAS experiment in Figure 8 and the static powder experiment in Figure 11 are plotted in Figure 12 as a function of time. The solid curves in Figure 12 were calculated numerically using eqs 11–21 and the same parameter set determined in the previous section. It is evident that the decay of magnetization is nonexponential in the case of the static powder and slower than in the MAS experiment. As mentioned in the theoretical section, there is almost no difference between the curves calculated for the isotropic and MAS conditions. This result justifies the use of eq 23.

Comparison of the Rate Constants of the DTAA Tautomerism Obtained by ^{15}N CPMAS NMR Line Shape Analysis and ^{15}N CPMAS T_1 Measurements. In order to compare the kinetic data obtained by line shape analysis and the T_1 method, each T_1 value was numerically converted using eq 23 into the corresponding rate constant k_{12} of the forward proton-transfer process defined in Figure 1 as mentioned above. For this purpose it was not necessary to assume an Arrhenius-type behavior of the rate constant. It was therefore possible to construct a single Arrhenius diagram from the data obtained by the different methods as shown in Figure 13. Fortunately, it was possible to obtain k_{12} values both from total line shape analysis as well as from T_1 analysis

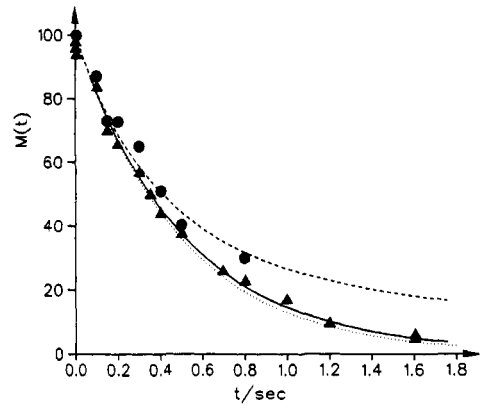

Figure 12. Plot of the integral signal intensities of Figures 8 and 11 as a function of time: (●, - - -) experimental and calculated values (using eq 23) for the static powder; (▲, —) experimental and calculated values (using eq 22) for the powder rotating at the magic angle; (···) calculated (using eq 23) for the case of isotropic longitudinal relaxation.

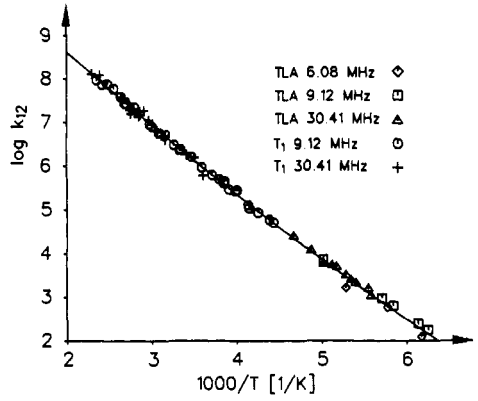

Figure 13. Arrhenius curve of the tautomerism of DTAA in the solid state.

in the milli- to microsecond range around 220 K. The agreement between both methods in this range is very satisfactory. This result is a further corroboration that the above-mentioned relaxation analysis is consistent.

On the other hand, it follows from Table 3 that the energies of activation as well as the preexponential factors of the DTAA tautomerism depend slightly on the temperature range where the rate constants are measured; i.e., the Arrhenius curve exhibits a slight concave curvature. This observation cannot arise from the use of two different methods for the determination of the rate constants because both methods agree very well in the overlapping temperature range. Therefore, we are convinced that the nonlinearity of the Arrhenius curve in Figure 13 is real. The simplest way to describe the curve is to use a sum of two exponentials

$$k_{12} = A^0_{12} \exp(-E^0_{a_{12}}/RT) + A^1_{12} \exp(-E^1_{a_{12}}/RT) \quad (32)$$

A nonlinear least-squares fit of the data leads to the values of log A^0_{12} = 10.3 ± 0.8, $E^0_{a_{12}}$ = 25.2 ± 2.4 kJ mol^{-1} and log A^1_{12} = 12.1 ± 0.2, $E^1_{a_{12}}$ = 33.5 ± 2.4 kJ mol^{-1}. The temperature dependence of the backward rate constants can be obtained by a combination of eqs 29 and 32. The agreement between experimental and calculated rate constants is very good as illustrated in Figure 13. Fitting the data to a simple Arrhenius equation gives the parameters $E_{a_{12}}$ = 29.1 ± 0.4 kJ mol^{-1} and log A_{12} = 11.5 ± 0.2. The error margins of these parameters are smaller than in the four-parameter case because the errors of the latter are interrelated. However, the least-squares sum is much smaller in the four-parameter case.

We omit a more detailed discussion of the origin of the nonlinearity of the Arrhenius curve but note that it might arise

according to Bell[40] from a contribution of proton tunneling. Tunneling is even manifest when analyzing the data in terms of the Arrhenius equation because the frequency factor obtained in this case is much smaller than 10^{13} s^{-1} as expected for a reaction where entropy does not change substantially along the reaction pathway.

Conclusions

It has been shown theoretically and experimentally that rate constants of millisecond to nanosecond proton transfers in crystalline powders can be determined by studying the longitudinal relaxation under CPMAS NMR conditions of heteronuclei whose dipolar interaction to the mobile protons is modulated by the proton transfer. The CPMAS conditions minimize systematic errors arising from orientation-dependent T_1 values in powders, signal-to-noise problems usually present in the NMR spectroscopy of heteronuclei, and enable the determination of the equilibrium constants necessary to interconvert the T_1 values into rate constants. In the future kinetic hydrogen/deuterium isotope effects could be measured by combination with ^2H NMR T_1 measurements performed on the static or rotating powders.

Acknowledgment. We thank the Deutsche Forschungsgemeinschaft, Bonn, and the Fonds der Chemischen Industrie, Frankfurt, for financial support.

References and Notes

(1) Universität Freiburg. Present address: Fa. Bayer AG, W-5900 Leverkusen, F.R.G.

(2) Gutowsky, H. S.; McCall, D. M.; Slichter, C. P. *J. Chem. Phys.* **1953**, *21*, 279. Kubo, R. *Nuovo Cimento Suppl.* **1957**, *6*, 1063. Sack, R. A. *Mol. Phys.* **1958**, *1*, 163. Binsch, G. *J. Am. Chem. Soc.* **1969**, *91*, 1304.

(3) Abragam, A. *Principles of Nuclear Magnetism*; Oxford University: New York, 1961.

(4) Ernst, R. R.; Bodenhausen, G.; Wokaun, A. *Principles of Nuclear Magnetic Resonance in One and Two Dimensions*; Clarendon Press: Oxford, 1987.

(5) Limbach, H. H. Dynamic NMR Spectroscopy in the Presence of Kinetic Hydrogen Deuterium Isotope Effects. In *NMR Basic Principles and Progress*; Berlin, 1990; Vol. 26, Chapter 2.

(6) Rumpel, H.; Limbach, H. H. *J. Am. Chem. Soc.* **1989**, *111*, 5429. Scherer, G.; Limbach, H. H. *J. Am. Chem. Soc.* **1989**, *111*, 5946. Schlabach, M.; Scherer, G.; Limbach, H. H. *J. Am. Chem. Soc.* **1991**, *113*, 3550.

(7) Meschede, L.; Gerritzen, D.; Limbach, H. H. *Ber. Bunsen-Ges. Phys. Chem.* **1988**, *92*, 469. Meschede, L.; Scherer, G.; Limbach, H. H. *Z. Naturforsch.* **1989**, *44A*, 459. Meschede, L.; Limbach, H. H. *J. Phys. Chem.* **1991**, *95*, 10267.

(8) Schaeffer, J.; Stejskal, E. O. *J. Am. Chem. Soc.* **1976**, *98*, 1031.

(9) Lyerla, J. R.; Yannoni, C. A.; Fyfe, C. A. *Acc. Chem. Res.* **1982**, *15*, 208.

(10) Fyfe, C. A. *Solid State NMR for Chemists*; C.F.C. Press: Guelph, Ontario, 1983.

(11) Mehring, M. *NMR—Basic Principles and Progress*; Springer-Verlag: Berlin, 1976; Vol. 11.

(12) Limbach, H. H.; Hennig, J.; Kendrick, R. D.; Yannoni, C. S. *J. Am. Chem. Soc.* **1984**, *106*, 4059.

(13) Limbach, H. H.; Gerritzen, D.; Rumpel, H.; Wehrle, B.; Otting, G.; Zimmermann, H.; Kendrick, R. D.; Yannoni, C. S., in Sixl, H., Friedrich, J., Bräuchle, C. *Photoreaktive Festkörper*, Karlsruhe: M. Wahl Verlag, 1985; pp 19–43.

(14) (a) Limbach, H. H.; Wehrle, B.; Zimmermann, H.; Kendrick, R. D.; Yannoni, C. S. *J. Am. Chem. Soc.* **1987**, *109*, 929. (b) Wehrle, B.; Aguilar-Parrilla, F.; Limbach, H. H. *J. Magn. Reson.* **1990**, *87*, 584. (c) Aguilar-Parrilla, F.; Wehrle, B.; Bräunling, H.; Limbach, H. H. *J. Magn. Reson.* **1990**, *87*, 592.

(15) Limbach, H. H.; Wehrle, B.; Zimmermann, H.; Kendrick, R. D.; Yannoni, C. S. *Angew. Chem.* **1987**, *99*, 241; *Angew. Chem., Int. Ed. Engl.* **1987**, *26*, 247.

(16) Wehrle, B.; Limbach, H. H.; Köcher, M.; Ermer, O.; Vogel, E. *Angew. Chem.* **1987**, *99*, 241; *Angew. Chem., Int. Ed. Engl.* **1987**, *26*, 934.

(17) Smith, J. A. S.; Wehrle, B.; Aguilar-Parilla, F.; Limbach, H. H.; Foces-Foces, M.; Cano, F. H.; Elguero, J.; Baldy, A.; Pierrot, M.; Khurshid, M. M. T.; Larcombe-McDuall, J. B. *J. Am. Chem. Soc.* **1989**, *111*, 7304.

(18) Wehrle, B.; Zimmermann, H.; Limbach, H. H. *Ber. Bunsen-Ges. Phys. Chem.* **1987**, *91*, 941. Wehrle, B.; Zimmermann, H.; Limbach, H. H. *J. Am. Chem. Soc.* **1988**, *110*, 7014.

(19) Wehrle, B.; Limbach, H. H. *Chem. Phys.* **1989**, *136*, 223.

(20) Hennig, J.; Limbach, H. H. *J. Magn. Reson.* **1982**, *49*, 322. Limbach, H. H.; Wehrle, B.; Schlabach, M.; Kendrick, R. D.; Yannoni, C. S. *J. Magn. Reson.* **1988**, *77*, 84.

(21) Szeverenyi, N. M.; Bax, A.; Maciel, G. E. *J. Am. Chem. Soc.* **1983**, *105*, 2579.

(22) Baldy, A.; Elguero, J.; Faure, R.; Pierrot, M.; Vincent, E. J. *J. Am. Chem. Soc.* **1985**, *107*, 5290.

(23) Frydman, L.; Olivieri, A. C.; Diaz, L. E.; Frydman, B.; Morin, F. G.; Mayne, C. L.; Grant, D. M.; Adler, A. D. *J. Am. Chem. Soc.* **1988**, *110*, 8336.

(24) Frydman, L.; Olivieri, A. C.; Diaz, L. E.; Frydman, B.; Kustanovich, I.; Vega, S. *J. Am. Chem. Soc.* **1989**, *111*, 7001.

(25) Frydman, L.; Olivieri, A. C.; Diaz, L. E.; Valasinas, A.; Frydman, B. *J. Am. Chem. Soc.* **1988**, *110*, 5651.

(26) Look, D. C.; Lowe, I. J. *J. Chem. Phys.* **1966**, *44*, 3437.

(27) Andrew, E. R.; Latanowicz, L. *J. Magn. Reson.* **1986**, *68*, 232.

(28) Meier, B. H.; Graf, F.; Ernst, R. R. *J. Chem. Phys.* **1982**, *76*, 767.

(29) Nagaoka, S.; Terao, F.; Imaschiro, F.; Saika, A.; Hirota, N. *J. Chem. Phys.* **1983**, *79*, 4694.

(30) Meyer, R.; Ernst, R. R. *J. Chem. Phys.* **1990**, *93*, 5518.

(31) Heuer, A.; Haeberlen, U. *J. Chem. Phys.* **1991**, *95*, 4201.

(32) Takeda, S.; Chihara, H.; Inabe, T.; Mitani, T.; Marauyama, *Chem. Phys. Lett.* **1992**, *189*, 13.

(33) Robyr, P.; Meier, B. H.; Ernst, R. R. *Chem. Phys. Lett.* **1991**, *189*, 471.

(34) Lorch, E.; Breitmaier, E. *Chem. Z.* **1975**, *99*, 87.

(35) Kendrick, R. D.; Friedrich, S.; Wehrle, B.; Limbach, H. H.; Yannoni, C. S. *J. Magn. Reson.* **1985**, *65*, 159.

(36) Torchia, D. A. *J. Magn. Reson.* **1978**, *30*, 613.

(37) Du Bois Murphy, D. J. *J. Magn. Reson.* **1986**, *70*, 307.

(38) Goedken, V. L.; Pluth, J. J.; Peng, S. M.; Bursten, B. *J. Am. Chem. Soc.* **1976**, *98*, 8014.

(39) Hoelger, Ch.; Limbach, H. H. Submitted for publication.

(40) Bell, R. P. *The Tunnel Effect in Chemistry*; Chapman and Hall: London, 1980.